CHARACTERIZATION OF HIGH-ENERGY HEAVY-ION IMPLANTED InP CRYSTALS BY A VARIETY OF TECHNIQUES*

F. XIONG, C. W. NIEH, T. A. TOMBRELLO, D. N. JAMIESON, T. VREELAND, JR., and M. A. NICOLET

Divisions of Physics, Mathematics, and Astronomy, 200-36
and Engineering and Applied Sciences
California Institute of Technology
Pasadena, California 91125

ABSTRACT

MeV ion implantation into InP compound semiconductor crystals with 5 MeV nitrogen ions has been investigated. The subsequent characterization was undertaken by a variety of techniques such as nuclear resonant reaction analysis, channeling Rutherford backscattering spectrometry, x-ray rocking curve measurement, and cross-sectional transmission electron microscopy. These techniques have clearly revealed substantial changes in structural properties and radiation-induced damage distribution as well as the influence of post-implantation annealing in ^{15}N ion-implanted InP samples. The results from these measurements, which are presented in this paper, are shown to be consistent with each other, and have led to a coherent description of the effects of the implantation and subsequent annealing. In a practical sense this has demonstrated the complementary nature of the analytical capabilities of all of these techniques used for the investigation of the processes involved in high-energy heavy-ion implantation.

This paper presented at the International Symposium on Application of Ion Beam Produced by Small Accelerators, Jinan, Shandong, China, October 20-24, 1987.

*Supported in part by the National Science Foundation [DMR84-21119].

ONE OF THE BROWN BAG PREPRINT SERIES
IN BASIC AND APPLIED SCIENCE

December 1987

I. INTRODUCTION

As is well known, ion implantation has been widely used as a very powerful technique for semiconductor doping and surface modification as well as device fabrication[1]. However, MeV ion implantation is especially envisioned to have potential in 3-dimensional device processing, buried layer formation, and modification of optical and electrical properties, etc. Application of low energy (keV) ion implantation to Si device fabrication has become standard technology in the Si industry[2]. It is extremely useful and important in III-V compound semiconductor technology, since the alternative method, thermal diffusion processing, is rather hard to control. Application of ion implantation to GaAs has achieved great success in the fabrication of GaAs FETs and integrated circuits[3,4], but application to InP is just at the beginning stage, in good part because the potentialities of this compound in device technologies have been widely recognized for only about ten years.

For conditions of practical importance, the damage as well as associated physical processes during the ion implantation are severe. A good understanding of the nature of those processes is crucial for appropriate applications of ion implantation. Work on GaAs can be found in many reports[5-7], but there are few reports on InP[8-10]. It is the purpose of our research to investigate further the physical processes involved and get a good understanding of the mechanism of the transient thermal processesing and damage production that occurs in the high-energy heavy-ion implantation into III-V compound semiconductors.

We have undertaken to study by a variety of techniques the radiation damage and crystal structure changes in MeV-nitrogen-ion implanted InP crystals as well as the influence of post-implantation annealing. The distribution of the implanted ions was determined by using nuclear resonant reaction analysis (NRRA). Radiation damage and strains induced by the implanted ions were measured with the x-ray rocking curve technique (XRC). Channeling Rutherford backscattering spectrometry (CRBS) and cross-section transmission electron microscopy (XTEM) have been employed to observe the structural changes and radiation-induced defect distribution in the as-implanted and subsequently annealed crystals. The results from these measurements are shown to be consistent with each other. In this paper, the experimental results of this implantation and characterization study are presented in detail. The radiation damage process and the mechanism of amorphization and recrystallization through implantation and thermal annealing are discussed briefly.

II. EXPERIMENTS AND RESULTS

II.1. Sample Preparation.

The samples used in this study were n-type InP single crystalline wafers. They were 0.5 mm thick with a polished surface in the (100) orientation with an Sn-doping

concentration of $7\times10^{16}/cm^3$. The ion implantaion was done with the Caltech 6 MV EN-tandem accelerator. To make profiling easier the rare isotope ions, $^{15}N^{2+}$, were generated at an energy of 5 MeV, uniformly defocused and projected onto the sample through a 6×6 mm^2 collimator. The samples were irradiated at ambient temperature onto the front polished surfaces at a beam flux of 0.5~0.8 $\mu A/cm^2$. The doses ranged from 5×10^{13} to 5×10^{16} ions/cm^2. During implantation, the sample was tilted about 5~7 degrees to minimize the possible channeling effect. The beam flux had to be limited to under $1\mu A/cm^2$ to prevent sample melting.

Post-implantation annealing was done using a graphite strip heater for 20 minutes with an ambient H_2 gas flow. Samples were set in the face-to-face configuration with a large piece of virgin InP crystal covering the implanted sample surfaces. This provides a local phosphorus pressure to prevent dissociation of InP occuring near the surface during high temperature annealing. The temperature of about 500C was chosen, based on the previous XRC results of isochronal annealing, which showed completed strain recovery on Cl-ion-irradiated InP at temperatures higher than 450C[6]. This was also observed on ^{15}N-ion-implanted samples in this study (see section II.4)

II.2. Implant Depth Profiling by NRRA

To locate precisely the implanted nitrogen with depth, the resonant reaction $^{15}N(p, \alpha\gamma)^{12}C$ at a proton energy of 897 keV was employed to profile the ^{15}N implanted into InP crystals. The reaction products of 4.43 MeV γ-rays were detected by a NaI(Tl) scintillation detector. The experimental set-up was the same as that used for hydrogen depth profiling, as described in detail in ref. 11. The measured depth profiles are shown in Fig. 1 where the depth scale is converted from the corresponding incident proton beam energy with the stopping power, which can be estimated basing on the InP density of 3.95×10^{22} atoms/cm^3 and stopping cross sections for single-element solids found in standard references[12]. The yields were normalized by setting the integrated yield under the peak to be equal to the implanted doses. As expected, the profiles show a standard Gaussian-like distribution of ^{15}N implanted in InP with peaks centered at 3.71 μm, and they are dose-independent. The depths of these peaks mark the average depth range of the 5 MeV ^{15}N ions in the InP single crystal. The measured FWHM is shown to be 0.65 μm. Considering the energy straggling of MeV protons in InP, which can be estimated through the Bohr formula[13], to be 10 keV (~0.2 μm) at the depth 4μm in InP, then the real width of the implant distribution is about 0.6 μm. Slight peak broadening has been found in the annealed samples (profiles are not presented here), but the peak is still centered at the same position as that in the as-implanted sample. This indicates that only very small migration and diffusion of the implanted ^{15}N in InP were caused during the thermal annealing. In addtion, a

profile from the sample implanted with 8 MeV ^{15}N is presented in Fig. 1, illustrating the energy dependence of the depth range and the distribution width of the implanted ^{15}N in InP.

II.3. Damage Depth Profiling by CRBS

The channeling RBS experiments were performed with a $^4He^+$ beam using 3.5 MeV from the EN-tandem and 3 MeV from the 1MV-Pelletron. During channeling measurements, the samples were aligned along the $\langle 100 \rangle$ surface normal axis direction, and backscattered particles were detected by a solid detector at a lab angle of 170^o. The random spectra were obtained by tilting the sample about 7 degrees and rotating the sample continuously.

The typical resulting spectra from the as-implanted samples as well as annealed ones are illustrated in Figure 2. The lowest curve is a channeled spectrum from the non-irradiated sample, showing a minimum dechanneling yield from the residual defects in the virgin crystal. The curves in the middle are taken from the implanted sample with different doses as indicated beside the curves. As shown in the spectra, the ^4He particles suffered more and more de-channeling in the irradiated sample as they go deeper inside, which illustrates the depth distributions of the damage in the InP crystals induced through the implantation. One remarkable feature which has been clearly observed is that as the implant dose increases the dechanneling yield dramatically increases. At a certain depth inside the samples it saturates at about 100% when the dose is over $1 \times 10^{15}/cm^2$. This region gradually extends towards the sample surface with higher doses; this saturation is the indication of the formation of a buried amorphous layer as will be established by the XTEM micrograph. Note that the spectrum from the as-implanted sample at the dose of $1 \times 10^{16}/cm^2$ is not shown here, as it looks almost the same as the random spectrum except for a slight drop for a few hundred Å near the surface. This implies that at this dose an implantation-induced buried amorphous layer has formed from the end of the ion range to a place near the surface, where a heavily damaged layer begins. These have been clearly observed through the XTEM analysis (see Figures 4c and 4d). The results from those annealed samples, as presented in Fig. 2b, show a large decrease of the dechanneling yield near the surface region, indicating the recovery of the surface damage and defects through thermal annealing. However, on higher dose-implanted samples, the backscattering yields from the buried amorphous regions are still nearly as high as those of the random spectrum. These have been shown to correspond to the highly disordered region which is recrystallized from the original amorphous layer during high temperature annealing. All the results obtained by CRBS have been comfirmed by XTEM observations as shown in Section II.5.

II.4. Strain Measurement by the XRC Technique

The x-ray rocking curves from the (400) symmetrical diffraction were taken using a double-crystal diffractometer. In this case, perpendicular lattice strain has been measured. Figure 3 shows a set of rocking curves from InP(100) samples implanted with a variety of doses, ranging from 5×10^{13} to 5×10^{16} ions/cm^2. In the plots, the small peaks from the substrate contribution are centered at the zero point as references. The large peaks at positive angles are contributed by the radiation-induced strained surface layer and the buried amorphous-crystalline interfaces. The postive angular shift of these strain peaks indicates, as we reported earlier[8], that a lattice spacing contraction has occurred in the plane parallel to the surface. This is opposite to the case of GaAs(100) as reported by Wie et al.[6]. It has been found that implanted ions have disordered the lattice structure and gradually induced lattice strain inside the crystal, with a saturation at the perpendicular strain level of $0.060\pm0.002\%$ when the implant dose is greater than 2×10^{15} ions/cm^2. Comparing with the results by CRBS and XTEM, it can be concluded that the Bragg diffraction angle broadening and lattice-strain production reveal the dose-dependent nature of the crystal damage and lattice variation induced by ion irradiation during the implantation, and that the strain saturation indicates the occurrence of implantation-induced amorphization. In addition, one noticeable feature which can been clearly observed from the XRCs of those samples implanted with very high doses, is that the levels of saturated strain have decreased when the dose is over 1×10^{16}/cm^2. At those doses, as shown by CRBS and XTEM, the implantation-induced amorphous layer has already approached the top surface. Thus the decrease might be a sign that in-situ annealing and recrystallization have occured inside the sample during implantation. The detailed damage and strain profiles can be extrated from the these XRCs by theoretical simulation and fitting with the x-ray dynamical diffraction theory[6]. The calculated results (not presented here) obtained for InP are very similar to those for GaAs reported by Wie[6], except for the strain sign inversion.

The rocking curves taken from post-implantation, isochronically-annealed InP samples have shown that the radiation-induced strain in the implanted InP crystals has had a gradual recovery through the high temperature annealing, which is very similar to the results from the Cl-ion-implanted samples reported previously[8]. Complete recovery of strain occurs at 450C. A well-shaped peak from the damage-recoved surface appears at the exact position as the substrate peak, but the reflecting intensity has dropped to about half of that from a non-irradiated InP sample and the width has broadened. This is due to the absorption and scattering by the buried disordered layer deep inside the crystal formed through implantation and recrystalized through high-temperature annealing. This agrees very well with the XTEM data (see the next section).

II.5. Structure Characterization by XTEM

The XTEM experiments were performed using the Caltech's Phillips Model E430 TEM. Both as-implanted and subsequently annealed samples were prepared through a standard TEM sample preparation procedure[14] (mechanical thinning, dimpling and ion milling), but it was found to be rather difficult because the InP crystals, especially the implanted samples, are much more fragile than those of Si and GaAs. Reactive I^+ ion milling[15] has to be used since Ar ion milling causes preferential sputtering of phosphorus leaving minute metallic indium islands on the sample surface.

Figure 4 shows some bright field XTEM micrographs of the entire implanted regions of InP specimens which were implanted with different doses of (a) $5\times10^{14}/cm^2$, (b) $1\times10^{15}/cm^2$, and (c,d) $1\times10^{16}/cm^2$. Figures 4a, 4b and 4c are as-implanted. The sample surface (A) lies at the left-hand side in the micrograph. The regions (B) with irregular dark spots are found to be heavily damaged with a high density of point defect clusters induced by the ion implantation. The contrast-featureless bands (C) in the micrographs are the buried amorphous layers formed during implantation. Selected area diffraction patterns taken from those regions allow us to determine whether they are in the amorphous form or just heavily-damaged crystalline materials. It has been found that at doses below $5\times10^{14}/\mathrm{cm}^2$, only radiation damage with a high density of defect centers is induced in the region near the end of ion range, while on the samples implanted with a dose over $1\times10^{15}/\mathrm{cm}^2$ the amorphous layers have formed with their inner interfaces at a depth of about 4 μm, which is consistent with the NRRA implant depth profile data and the CRBS damage profiling data. It shows that the width of the buried layer gets broadened towards the sample surfaces when the dose increases, while the maximum depth is almost fixed, independent of the implantation doses. Fig. 4d. shows a bright field XTEM image taken from the annealed sample implanted with the dose of $1 \times 10^{16}/\mathrm{cm}^2$. Comparing with the micrograph of the as-implanted sample, the thermal annealing effect is clearly seen. The surface damage and defects have been greatly reduced, and recrystallization has emerged in the buried amorphous region (E), which consists of high densities of microtwins and stacking faults in the regions near two boundaries and polycrystalline structure in the central part. This interpretation has been confirmed by selected area diffraction patterns taken on the individual regions. It is important to notice that the boundaries between the buried layer and the substrate or the surface crystalline layer are sharp, which is different from what was observed on GaAs samples[7]. This is shown more clearly in the high resolution XTEM pictures.

Detailed characteristics on the structural changes caused by implantation and subsequent annealing have been studied through high resolution transmission electron

microscopy (HRTEM) analysis. The observations were performed in the [110] orientation at a magnification of 5×10^5. In this case, the lattice structure has been shown at the atomic scale, and a 3.4 Å separation between lattice arrays is seen very clearly. Fig. 5 shows lattice image from the damaged region near the end of the ion range in a low-dose-implanted sample ($5\times10^{14}/cm^2$). The one from the as-implanted specimen (Fig. 5a) shows radiation-induced defects of a very high density, appearing in dislocation loops, stackfaults and point defect clusters, while in the annealed sample (Fig. 5b) similar defects at a lower density have been seen. As shown in Fig. 6a, in the high-dose-implanted sample ($1\times10^{16}/cm^2$), a buried amorphous layer has formed, and the amorphous/crystalline interface is very sharp. Some microtwins and stacking faults in a low density of microtwins appeared on the substrate crystal side. They might have been introduced by an in-situ thermal annealing effect during implantation. After the post-implantation annealing at high temperature, recrystallization occurs in the buried amorphous region, accompanied by defect recovery in the damaged crystalline region, as shown in Fig. 2b. Figure 6b is the HRTEM micrograph of the inner interface. It illustrates the typical annealing structure near the original amorphous/crystalline interfaces, where long-range microtwins and stacking faults have formed, starting at the interfaces and extended towards the implantation-induced amorphous band inside. The similar structure has been observed in the top interface.

III. DISCUSSION AND SUMMARY REMARKS

The experiments have clearly revealed substantial changes in structural properties as well as radiation-induced damage distributions and build-up with increasing the implantation dose in the ^{15}N ion implanted InP samples. This has demonstrated the complementary nature of the analytical techniques used for the investigation of the processes involved in the high-energy heavy-ion implantation, and led to a good understanding of the mechanism of MeV ion implantation-induced amorphization and subsequent annealing-stimulated recrystallization in InP compound semiconductors. Several interesting features of MeV-ion-implanted InP crystals and the relationship between the distribution of implants, the radiation-induced damage profile and the amorphized region in the implanted sample as well as the influence of post-implantation annaealing effects have been found. NRRA depth profiling precisely measures the depth range of implanted 5 MeV nitrogen,which is centred at 3.71μm deep with a Gaussian-like distribution. The combination of CRBS and XTEM illustrates consistently the implantation-induced damage profile and the structure transition as well as the influence of subsequent thermal annealing. The damage was found to be distributed all along the ion transport path with maximum depth at 4μm, where the implanted ^{15}N concentration is at its half maximum on the inner boundary. For implantation at doses over $1\times10^{15}/cm^2$, amorphization has occured, starting from the heavily damaged

region where the energetic incident ions stop (nuclear stopping region). The buried amorphous layer extends towards the sample surface as the implanted dosage increses. We classify the proceses involved in the high energy implantation as electronic and nuclear spikes. The electronic spike is generated by electronic cascade collisions in the high energy range and causes electronic damage and point defects. The nuclear spike occurs in the low energy range where the ions stop due to nuclear collisions, by which the crystal suffers direct damage. The amorphous layer forms when the defect density is over a critical threshold. Subsequent high temperature annealing causes the amorphous layer to recrystalize and the damaged layer to reorder through complex thermal processes, as shown by the CRBS and XTEM results. The XRC sensitively measures the implantation-induced lattice strain; the observed strain saturation is related to the occurrence of the amorphization. Detailed data analysis of all these measurements and the investigation of the mechanism of implantation-induced amorphization and annealing-stimulated recrystallization will be presented elsewhere[16].

We would like to note here that electrical measurment of the I-V characteristic curves has also performed on both as-implanted and annealed samples. We have found that high resistivity has been stimulated and increases along with the implanted dose. Buried semi-insulating layers, which one hopes should form by high dose nitrogen ion implantation, may be very useful for fabricating optical laser devices[17]. The results of the electrical study of MeV-nitrogen-ion implanted InP and its application to device fabrication will reported later[18].

REFERENCES

1. D. C. Ingram, Nucl. Instr. and Meth. B12 (1985) 161, and references therein.
2. O. W. Holland, J. Narayan and D. Fathy, Nucl. Instr. and Meth. B7/8 (1985) 243, and references therein.
3. F. Eisen, C. Kirkpatrick, and P. Asbeck, in *GaAs FET Principles and Technology*, ed by J. V. Dilorenzo and D. D. Khandelwal, published by Artech House, Inc., (1982) p117-p144, and references therein.
4. Hidetoshi Nishi, Nucl. Instr. and Meth., B7/8 (1985) 395.
5. D. K. Sanada, T. Sands and J. Washburn, Appl. Phys. Lett. 44(6) (1984) 623.
6. C. R. Wie, T. Vreeland, Jr. and T. A. Tombrello, Nucl. Inst. and Meth. B16 (1986) 44; Phys. Rev. B33 (1986) 4083; J. Appl. Phys. 59 (1986) 3743.
7. T. T. Bardin, J. G. Pronko, F. A. Junga, W. A. Opyd, A. J. Mardinly, F. Xiong and T. A. Tombrello, Nucl. Instr. and Meth. B24/25 (1987) 548.
8. C. R. Wie, T. Jones, T. A. Tombrello, T. Vreeland, F. Xiong, Z. Zhou, G. Burns and F. H. Dacol, Mat. Res. Soc. Symp. Proc., Vol. 74 (1987) 517.
9. M. Slater, S. Kostic, M. J. Nobes and G. Carter, Nucl. Instr. and Meth., B7/8 (1985) 429.
10. D. K. Sadana, Nucl. Instr. and Meth., B7/8 (1985) 375, and references therein.
11. Fulin Xiong, F. Rauch, Chengru Shi, Zhuying Zhou, R. P. Livi, and T. A. Tombrello, Nucl. Instr. and Meth. B27 (1987) 432.
12. H. H. Andersen and J. F. Ziegler, *Hydrogen Stopping Powers and Ranges in All Elements*, in *The stopping and Ranges of the Ions in Matter,* Vol. 3, ed by J. F. Ziegler, published by Pergamon Press Inc., 1977.
13. See discussions in Section 3.1 in ref. 2 and references therein.
14. J. C. Bravman and R. Scinclair, J. Electron Microscope Tech. 1 (1984) 53.
15. N. G. Chew and A. G. Cullis, Appl. Phys. Lett. 44(1) (1984) 142.
16. F. Xiong, T. A. Tombrello, C. W. Nieh, T. Vreeland, D. N. Jamieson, and M. A. Nicolet, to be presented at 1987 Fall meeting of American Materials Reseach Society.
17. T. R. Chen, at Caltech, private communication.
18. F. Xiong, H. Wang, T. R. Chen, and T. A. Tombrello, to be published.

FIGURE CAPTIONS

Fig. 1. Depth profiles of ^{15}N by NRRA in the InP crystals implanted with 5 MeV ^{15}N in the doses of $2\times10^{16}/cm^2$ (+ points) and $5\times10^{16}/cm^2$ ($\times$ points). The Gaussian-like distributions were found with a depth centered at 3.71 μm and a width of 0.65 μm and were independent of dose. The solid curves is calculated by standard Gaussian function with parametes as listed. The profile with o points is taken from the sample implanted with 8 MeV ^{15}N, illustrating the energy dependence of the depth range and width.

Fig. 2. Channeling RBS spectra of InP crystals implanted with 5 MeV ^{15}N at room temperature with a sequence of doses as marked beside the curves, (a) as-implanted, (b) annealed. See details in the text.

Fig. 3. X-ray rocking curves of the 5MeV-^{15}N-ion-implanted InP from (400) symmetrical diffraction with respect to the InP substrate. The radiation-induced strain and the strain saturation are shown. See details in the text.

Fig. 4. XTEM micrographs of ^{15}N ion implanted InP specimens on the entired implanted regions with different doses: (a) $5\times10^{14}/cm^2$, as-implanted, (b) $1\times10^{15}/cm^2$, as-implanted, (c) $1\times10^{16}/cm^2$, as-implanted, and (d) $1\times10^{16}/cm^2$, annealed. As marked in the figure, A is the surface region; B, heavily damaged region; C, amorphous region; D, substrate crystal; and E, recrystallized region. See details in the text.

Fig. 5. HRTEM micrographs of the radiation-induced damage region in low dose implanted samples: (A) as-implanted, where a high density of implantation-induced defects (stacking faults and dislocation loops) is shown; (B) annealed, where the defect density has decrease dramatically and only a few stacking faults on {111} directions are presented.

Fig. 6. HRTEM micrographs of the buried layer interface in high dose implanted samples: (A) as-implanted, where a sharp interface between the implantation-induced amorphous zone and the crystalline substrate is shown; (B) annealed, where the thermal annealing structure through recrystalization in the original implantation-induced amorphous region is illustrated.

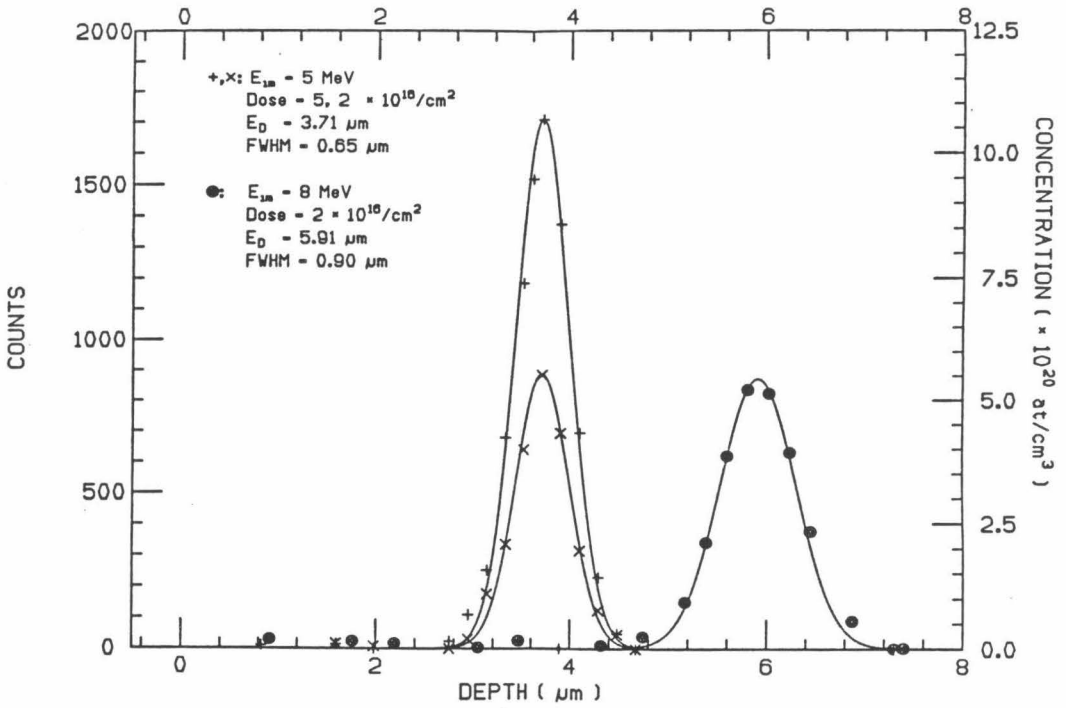

Figure 1.

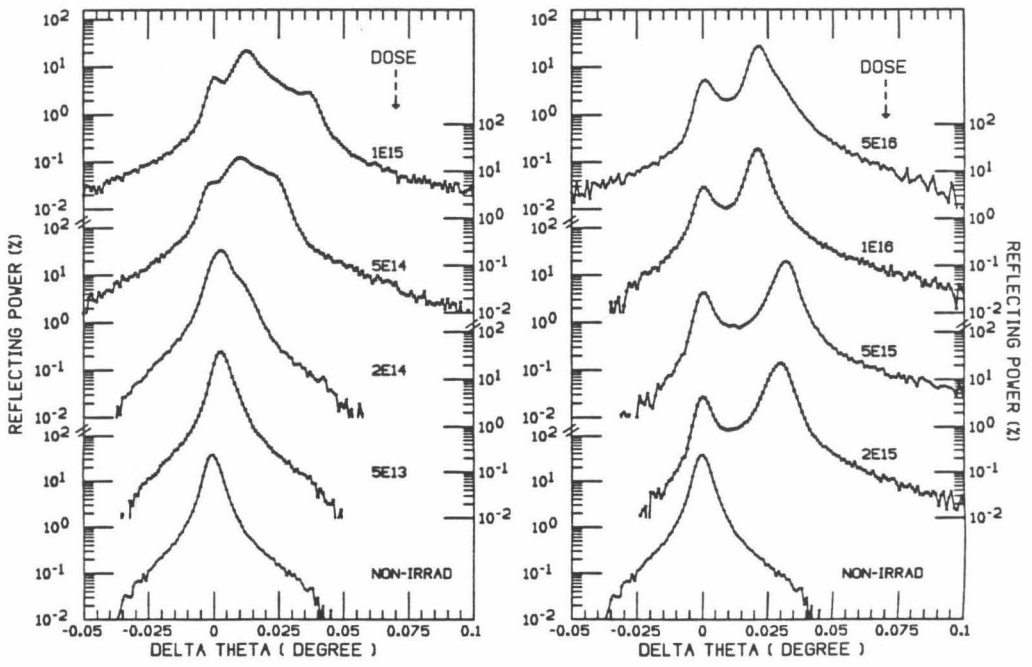

Figure 3.

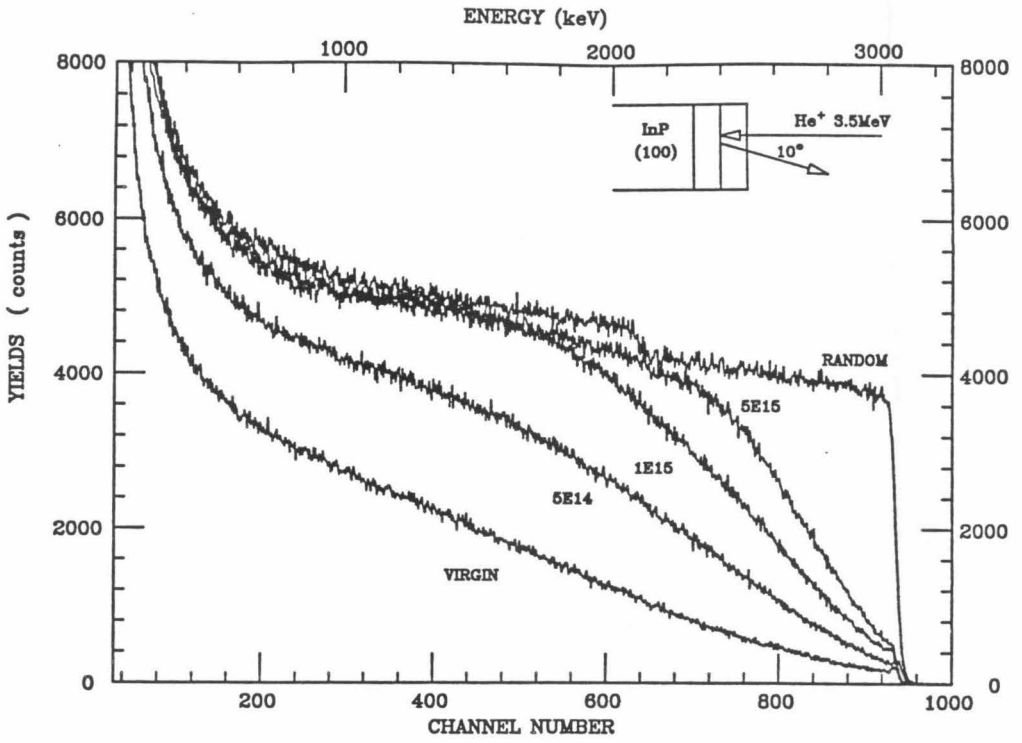

FIGURE 2a

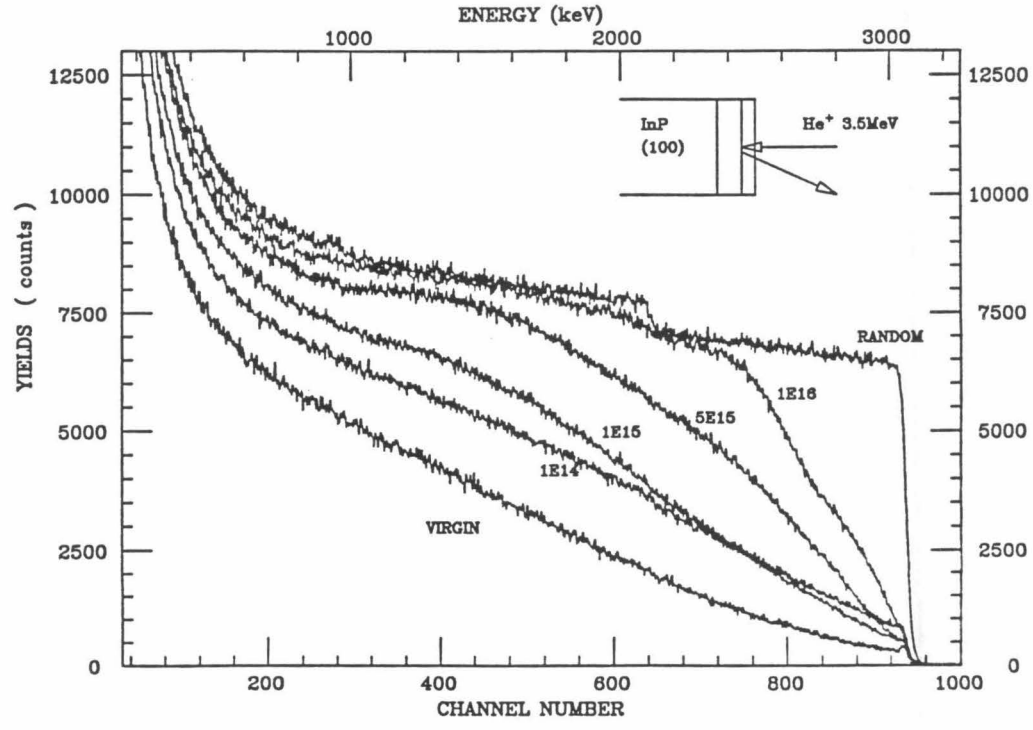

FIGURE 2b

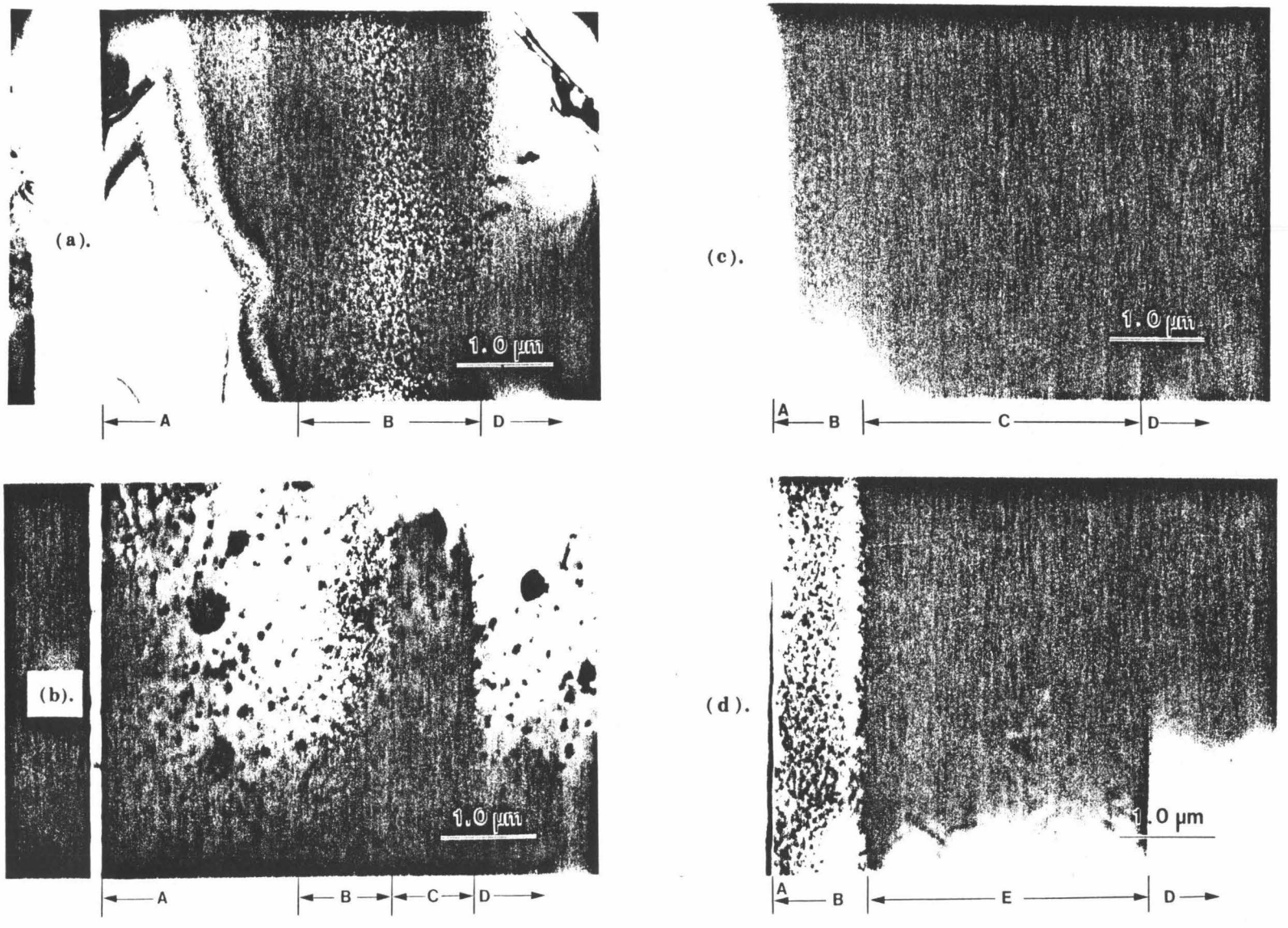

Figure 4.

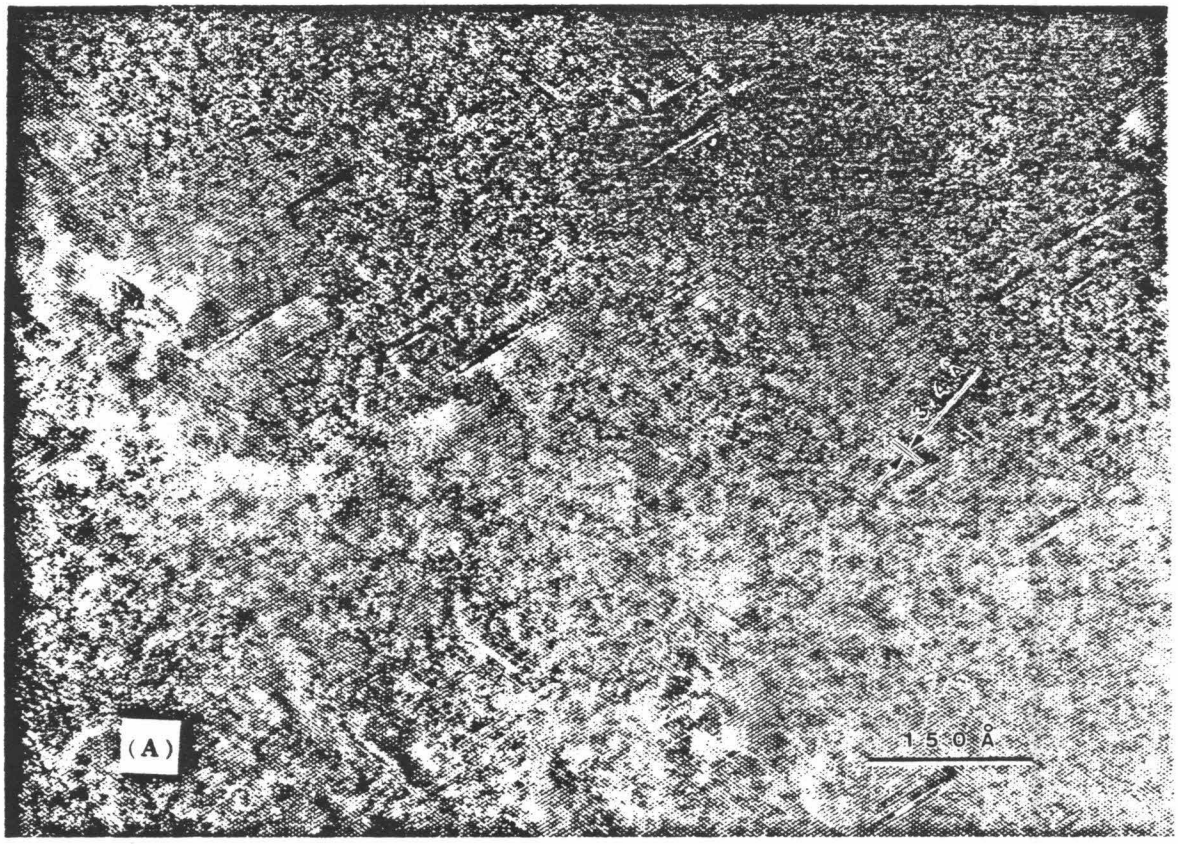

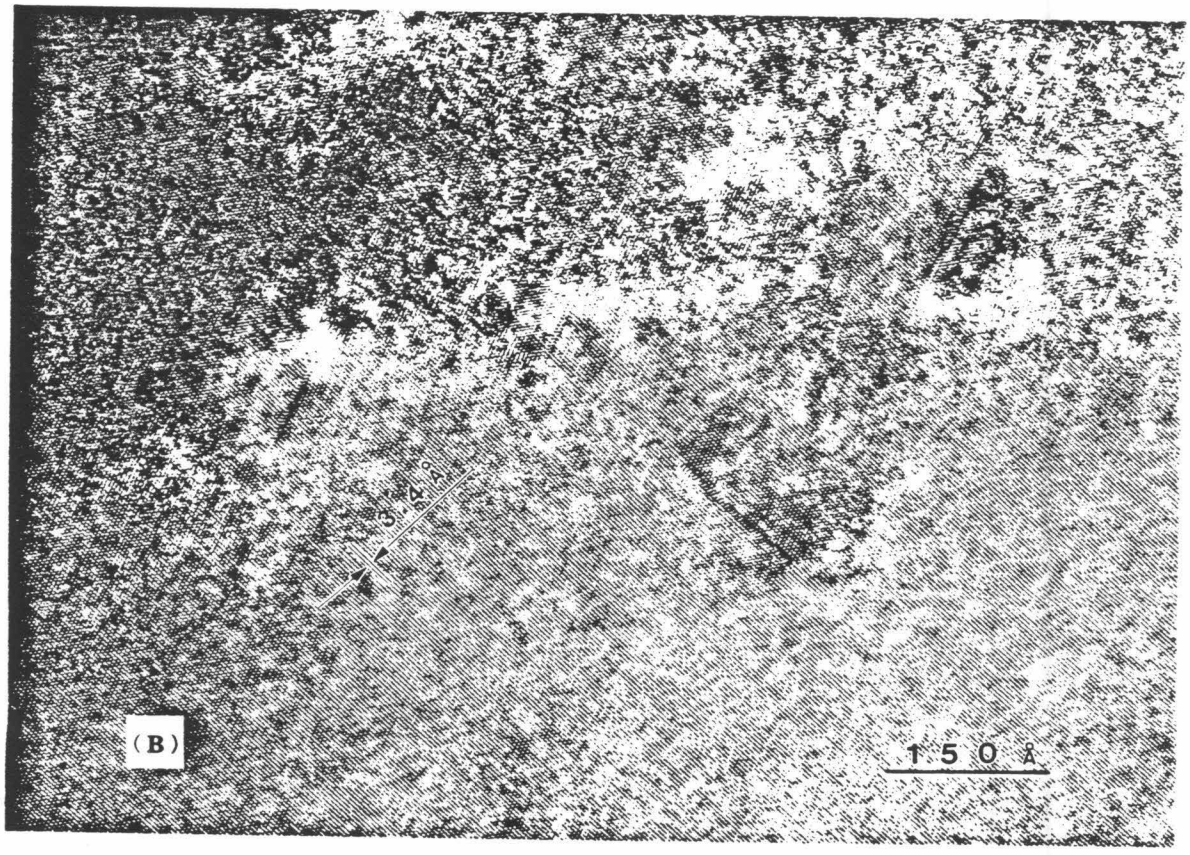

Figure 5.

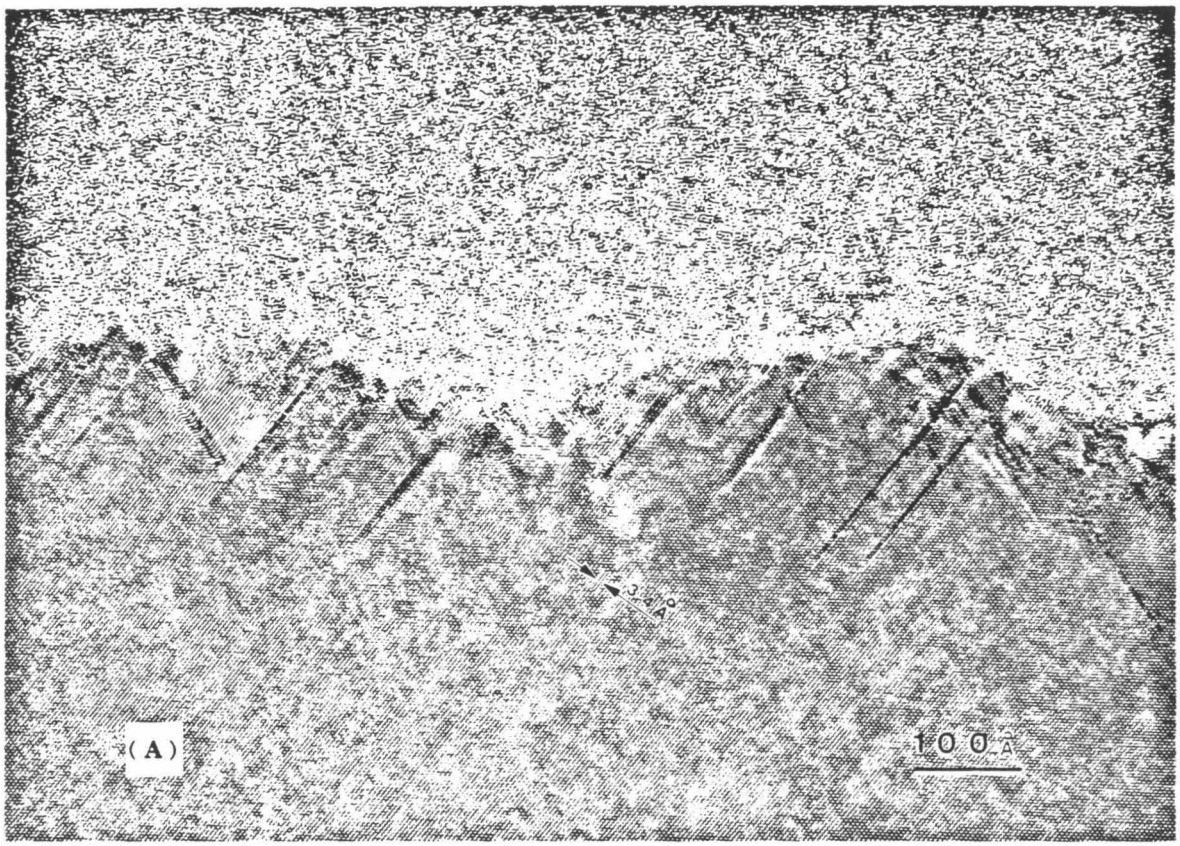

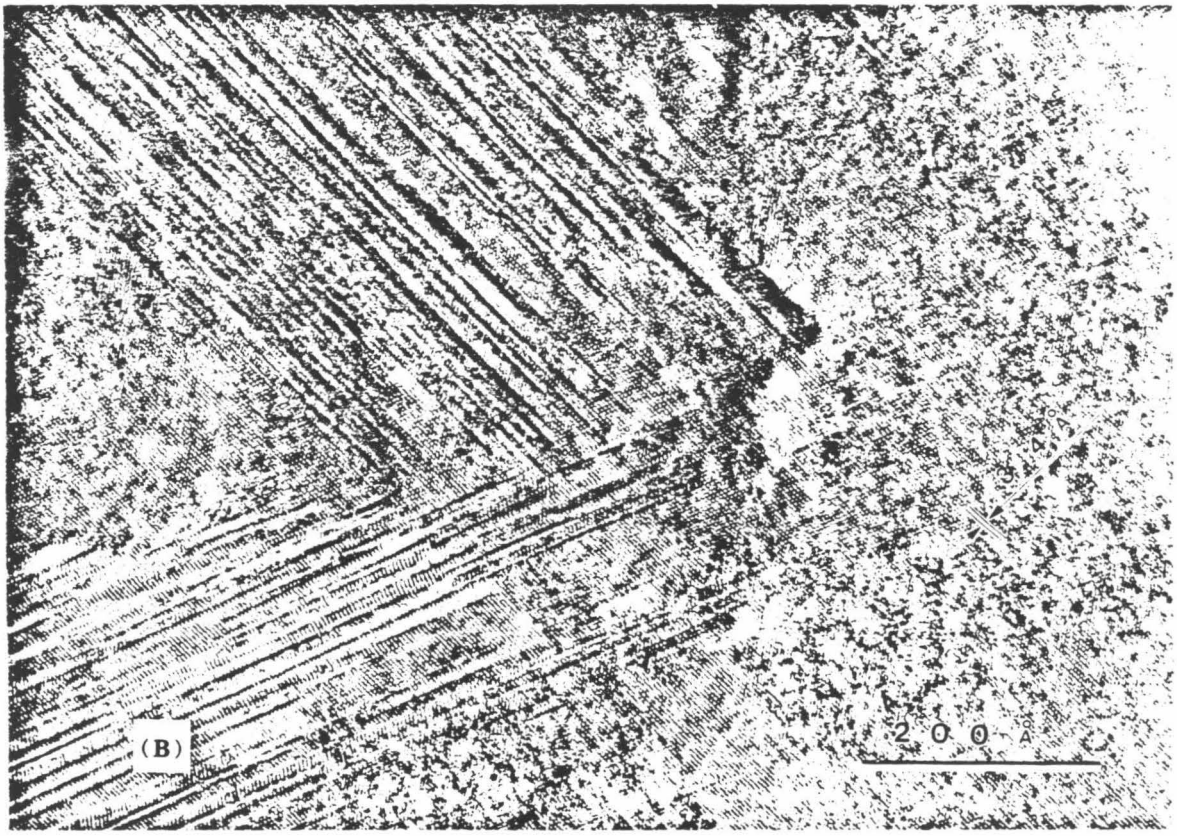

Figure 6.

BROWN BAG PREPRINT SERIES

BB-45 Computer Simulation of the Mechanical Sorting of Grains
BB-46 Feedback in Wind-Blown Sand Transport
BB-47 Scratching the Surface
BB-48 Computing with Particles
BB-49 Faunal Sorting of Sediments: Some Experiments with Desert Beetles Genus (Eleodes)
BB-50 The Impact Process in Eolian Saltation: Two-Dimensional Studies
BB-51 The Ubiquity of C-H Bond Breaking by MeV Ion Irradiation
BB-52 Electrical and Structural Changes in GaAs Crystals from High-Energy, Heavy-Ion Implants
BB-53 Hydrogen Depth Profiling in Solids: A Comparison of Several Resonant Nuclear Reaction Techniques
BB-54 Response of Desert Pavement to Surface Disturbances
BB-55 Simulation Studies of Collision Cascades in Liquid In Targets
BB-56 A Theoretical Model for Eolian Impact Ripples
BB-57 Radiation Defect-Induced Lattice Contraction of InP
BB-58 A Study of Surface Effects and Hydrogen Distribution in Glassy Zr-Rh Alloys
BB-59 A Continuum Theory of Granular Flow Including Spin
BB-60 A Physical Model of Wind-Blow Sand Transport
BB-61 Simulation of Isotopic Mass Effects in Sputtering, II
BB-62 Radiation Damage in Vitreous Fused Silica Induced by MeV Ion Implantation
BB-63 Photoreflectance, Absorption, and Nuclear Resonance Reaction Studies of $Al_xGa_{1-x}As$ Grown by Molecular Beam Epitaxy
BB-64 Direct Determination of Al Content in MBE Grown $Al_xGa_{1-x}As$ ($0 \leq x \leq 1$) by NRRA and XRC Techniques